Highly Efficient, Self-Powered UV Photodiodes based on Leadfree Perovskite Nanocrystals through Interfacial Engineering

Xiaoyu Huang[1,2], Hong-Tao Sun[1] and Naoto Shirahata[1,2,3,4]

[1] Research Center for Materials Nanoarchitectonics (MANA), National Institute for Materials Science (NIMS), 1-2-1 Sengen, Tsukuba 305-0047, Japan
[2] Graduate School of Chemical Sciences and Engineering, Hokkaido University, Kita 13, Nishi 8, Kita-ku, Sapporo 060-0814, Japan.
[3] Department of Physics, Chuo University, 1-13-27 Kasuga, Bunkyo, Tokyo 112-8551, Japan
[4] CNRS–Saint-Gobain–NIMS, IRL3629, Laboratory for Innovative Key Materials and Structures, National Institute for Materials Science, 1-1 Namiki, Tsukuba, Ibaraki 305-0044, Japan

E-mail: SHIRAHATA.Naoto@nims.go.jp

Abstract

Double perovskite crystals are promising alternatives for lead-based perovskites that has potential to address toxicity and instability issues. In this study, $Cs_2AgBiCl_6$ nanocrystals (NCs) with high absorption coefficients were synthesized by hot-injection method. The bandgap engineering was realized by tuning the halide composition in $Cs_2AgBiCl_6$ to $Cs_2AgBiBr_6$. Both NCs were used as light-absorbing layers in lead-free perovskite photodiodes that exhibit wavelength-selectivity for UV-visible light operatable even at a bias voltage of 0 V. $Cs_2AgBiBr_6$-based photodiode exhibits a characteristic detection peak at 340 nm with a responsivity of 3.21 mA/W, a specific detectivity up to 8.91×10^{10} Jones and a fast response speed with a rise/fall time of 30/35 msec. The excellent performance of self-driven photodiodes lights up the prospect of lead-free perovskite NCs in highly efficient optoelectronic devices.

Keywords: Double perovskite, Nanocrystals, Self-powered photodiode, Electron transport layer

Introduction

Recent years, metal halide perovskites (MHPs) synthesized by a simple solution process have demonstrated suitability in high-performance visible photodetectors [1–5] due to their large light absorption coefficients, high carrier mobility, long carrier diffusion lengths, and broad spectrum of light absorption.[6–10] Despite those great advantages, the lead toxicity and poor stability of some compositions have encouraged researchers to find lead-free alternatives. To be free from lead, the $A_2M^+M^{3+}X_6$ chemical formula materials such as $Cs_2AgBiCl_6$,[11] $Cs_2AgBiBr_6$,[12] $Cs_2AgInCl_6$,[13] and $Cs_2AgSbCl_6$ [14] were suggested as a promising strategy to replace two divalent Pb^{2+} ions with one monovalent ion M^+ and a trivalent ion M^{3+}.[15,16] These double perovskites possess tunable band gaps, smaller effective masses of electrons and holes, and high conductivity to efficiently transport and extract charges similar to lead-based perovskites.[17–19] The excellent properties make the double perovskite applied in various research fields, such as LED, photo detection, memory, and solar cell.[11,20–22] Among the suggested double perovskites, $Cs_2AgBiCl_6$ and $Cs_2AgBiBr_6$ has been recognized as favourable candidates for light-absorption layers in photovoltaic devices due to their excellent structural stability, long carrier recombination lifetime with thermal and humidity stabilities.[23,24] Those research achievements further confirm that the use of double perovskites is one of the most popular directions in the lead-free solar cells. However, $Cs_2AgBiBr_6$ and $Cs_2AgBiCl_6$ have natural hindrance factors that limit the

performance of photoelectronic conversion due to their large exciton binding energy of 220 meV,[25] and 333 meV.[26] Besides, the energy band mismatch with electron transport layer materials leads to non-radiative recombination and a large energy loss at the surface, yielding a poorer photoelectronic conversion efficiency.

Thus, it is crucial to select and adopt proper electron transfer layers (ETLs) with high mobility, low-defect state, and a suitable energy level arrangement for accelerating injection and transport of electrons to enhance the device performances of perovskite-based photodetectors. Until now, the ETL materials in perovskite photodetectors were generally metal oxides such as ZnO, TiO_2, and SnO_2.[27–29] Zhang et al. reported that modifying the number of layers ZnO to change the hydrophobicity, thereby fabricated the pinhole-free high efficiency perovskite solar cells.[30] Although ZnO is usually used as an ETL material due to its high electron mobility and low fabrication temperature, the low hydrophilic property of ZnO surface gives rise to a poor coverage film by creating pinholes.[31,32] In addition, the mismatched energy levels between the perovskite film and the ZnO ETL caused a large energy loss.[33,34] To overcome the shortcomings, the interface engineering at the heterojunction involves the construction of a bilayer or multi- layered ETL as a very critical technique.[35,36] For strategically constructed double ETLs with ZnO, we selected [6,6]-phenyl-C(61)-butyric acid methyl ester (PCBM), which has been reported to have a good band alignment with organic-inorganic lead perovskite films and to improve the power conversion efficiency of solar cells.[33]

In this study, we report on a self-powered ultraviolet (UV) photodiode where $Cs_2AgBiBr_6$ nanocrystals (NCs) are used as an active layer. In particular, the double ETL layers of PCBM/ZnO structure are investigated to reveal the effects of double ETLs on the enhancement of device performance. The insertion of polymer PCBM between ZnO and active layers allows formation of films with more well-matched energy levels for efficient electron transport. The $Cs_2AgBiBr_6$ NCs-based photodiode with PCBM/ZnO double ETLs exhibited outstanding detection performance compared to that of the single ETL device. The optimized photodiode exhibited a good self-powered device performance which acted as the responsivity of 3.1 mA/W when detectivity approached 8.91×10^{10} Jones, and a large light/dark current ratio near 200 was obtained. More importantly, spectral wavelength selectivity of $Cs_2AgBiBr_6$ NCs-based photodetector manifested the potential utilization in ultraviolet detection.

Experimental

Synthesis of $Cs_2AgBiCl_6$ and $C_2AgBiBr_6$ nanocrystals

Cesium acetate (CsOAc, 99.99%, Aldrich), silver acetate (AgOAc, 99%, Aldrich), bismuth(III) acetate (Bi(OAc)3, 99.99%, Aldrich), 1-octadecene (ODE, 90%, TCI), oleylamine (OLA, 70%, Aldrich), oleic acid (OA, 90%, Aldrich), chlorotrimethylsilane (TMCS, 98%, Aldrich), trimethylbromosilane (TMBS, 97%, Aldrich), hexane (96%, Wako) and ethyl acetate (99.5%, wako) were used without further purification.

The colloidal synthesis of NCs was performed using the reported protocol.[37,38] 1 mmol CsOAc, 0.45 mmol AgOAc and 0.5 mmol $Bi(OAc)_3$ were mixed with 10 mL ODE, 0.7 mL OLA and 2.8 mL OA on a 50 mL three-neck flask. The flask was connected to Schlenk line, then the mixture was heated to 110 °C and degassed for an hour. Then the heating temperature was raised by the speed of 6 °C/min, and when the temperature reached 165 °C, 0.4 mL TMCS was injected into the precursor solution. After 2 min of continuous heating, the reaction was stopped by immersing the flask into an ice water bath. When the temperature reached 30 °C, the reaction mixture was transferred into a centrifuge tube and centrifuged at 9000 rpm for 20 min. The supernatant was removed. Then the precipitate was dispersed in 5 mL hexane and centrifuged at 6000 rpm for 15 min, then the precipitate was discarded and the supernatant was mixed with ethyl acetate at the volume ratio of 1:1. Following a centrifugation process at 10000 rpm for 5 min. Finally, the precipitate was redispersed in hexane at the concentration of 25 g/mL for device fabrication. All the centrifugatios were conducted at 25 °C.

Materials characterization

The crystallinity was investigated by powder X-ray diffraction (XRD, Rigaku, Cu $K\alpha_1$), where the liquid sample was dropped on the silicon sample holder. High-resolution transmission electron microscopy (TEM) characterization was performed using a JEM-2100F2 instrument (JEOL) at 200 kV acceleration voltage. Scanning transmission electron microscopy coupled with energy dispersive spectroscopy (STEM-EDS) was utilized for the element analysis. Samples for the TEM analysis were prepared by drop-casting the 0.1 mg/mL hexane solution of NCs onto carbon-coated copper grids. Elemental analysis and chemical shift were studied by X-ray photoelectron spectroscopy (XPS, ThermoFisher), the samples for the XPS analysis were drop-casted on the silicon substrate. The absorption spectra was acquired with a JASCO V-650 UV-visible spectrometer. The LUMO and HOMO of nanocrystals were measured by ultraviolet photoelectron spectroscopy (UPS, ThermoFisher), the samples were prepared same with the XPS samples.

Device fabrication

A 10×20 mm^2 rectangle soda-lime glass covered with 150 nm thick ITO with a sheet resistance of 10~14 Ω/sq was used as the substrate. The ITO film was patterned to into a narrow strip about 2 mm wide and 20 mm long. ITO-covered glasses were cleaned by the detergent, deionized water, isopropanol, and acetone in ultrasonic cleaner successively (30 min for each

step). Next, organic contaminations on the substrate surface were removed exposure to vacuum ultraviolet (VUV) light (Ushio Inc., Japan, λ = 172 nm and 10 mW/cm^2) for 30 min under a reduced pressure of 1 kPa and N_2 flow, resulting in a super hydrophilic surface due to oxidation.[39] Then the substrates were transferred into the Ar-filled glove box where the oxygen and water levels are continuously monitored to maintain both O_2 < 1 ppm and H_2O < 1 ppm. 70 μL of an PEDOT:PSS solution was spin-coated on ITO glassed at a rate of 3000 rpm for 45 s and annealed at 150 ºC for 30 min. The NC solution was spin-coated onto PEDOT:PSS films at 1500 rpm for 45 s and annealed at 180 ºC for 10 min. PCBM solution was spin-coated onto the perovskite-coated films at 2500 rpm for 45 s and heated at 120 ºC for 10 min. Next, ZnO solution was spin-coated at 2500 rpm for 45 s and heated at 140 ºC for 30 min. Finally, Al electrode with a thickness of 170 nm was thermally evaporated onto ZnO films under the pressure of 5×10^{-5}.

Device measurement

The electrical characterization was done using Keithly 2425 Source Meter and KickStart software. Compact Xenon light source (300 W, Asahi Spectra Co., Ltd, MAX-301) combined with bandpass filters (310, 340, 365, 380, 410, 440, 470 and 490 nm) was used as light sources for different wavelengths. The peak linewidths of the incident light passing through the bandpass filters were 10 nm, respectively. The power of UV light at different intensities was recorded using a Laser power & energy meter (Ophir Optronics Solutions Ltd, NOVA II). All the light current density−voltage (I-V) curves were measured in ambient air at various conditions. For the I-V measurement, the dark current was measured without illumination for each device, the light current was measured after each scan of dark current under the illumination of a specific wavelength (310, 34, 365, 380, 410, 440, 470 and 490 nm) at a specific power intensity (range from 2~20 mW/cm^2) as needed. There was no obvious difference when we compared the dark current which was measured before the light current to that measured after the light current for same device. For the dynamic response measurement, the anode and cathode of the device were connected to a 1 GΩ load resistor and a digital oscilloscope (Iwatsu Electric Co., Ltd, DS-5624A) combined with an optical chopper (#55-783, Edmund Optics). The dynamic response displayed on the oscilloscope and the response time was extracted according to the record. All the device measurements were conducted in air and at room temperature.

Results and discussion

Figure 1(a) shows XRD patterns of $Cs_2AgBiCl_6$ and $Cs_2AgBiBr_6$ NCs. The presence of multiple diffraction peaks exhibited the structural characteristics of the nanocrystals. For $Cs_2AgBiCl_6$ NCs, domain diffraction peaks at 23.28°, 33.21°, 40.96°, and 47.64° were assigned to (022), (004), (224) and (044) diffraction planes of standard cubic double perovskite structure with a space group of Fm-3m. The estimated lattice parameter was 10.78 Å. Other peaks were consistent with the simulated values of $Cs_2AgBiCl_6$_11523 in the literature,[40] confirming the formation of double perovskite structure via the modified hot-injection method. For $Cs_2AgBiBr_6$ NCs, domain diffraction peaks at 15.49°, 22.06°, 27.32°, 31.60°, 39.00°, and 45.32° were assigned to (002), (022), (222), (004), (224) and (044) diffraction planes of standard cubic double perovskite structure with a space group of Fm-3m. The estimated lattice parameter was 11.31 Å. These diffraction peaks were consistent with the $Cs_2AgBiBr_6$_18989 in the literature.[41] The results of XRD indicated that the diffraction pattern of $Cs_2AgBiBr_6$ shifts to a low 2θ angle side compared to $Cs_2AgBiCl_6$, wherein the lattice expansion could be resulted from the larger ionic radius of Br- (1.96 Å) compared to Cl^- (1.81 Å). HR-TEM images of $Cs_2AgBiCl_6$ and $Cs_2AgBiBr_6$ NCs are shown in **Figure 1(b)-(c)**. The mean diameters of the NCs were 10.83 ± 3.60 nm and 9.88 ± 2.40 nm for $Cs_2AgBiCl_6$ and $Cs_2AgBiBr_6$ samples, respectively. The inset shows the

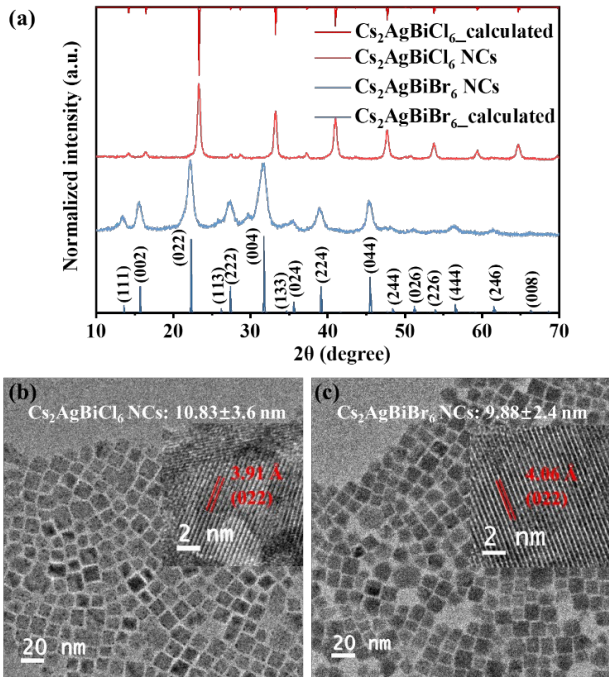

Figure 1. (a) X-ray diffraction (XRD) patterns of $Cs_2AgBiCl_6$ and $Cs_2AgBiBr_6$ NC samples. HR-TEM images of (b) $Cs_2AgBiCl_6$ NCs and (c) $Cs_2AgBiBr_6$ NCs. The inset figures are enlarged images that show the lattice spacing of the individual NCs.

enlarged images of the representative NCs. It could be seen that the interplanar spacing of (022) is consistent with the XRD results which indicate the lattice expansion when the halide ion in double perovskite changed from Cl^- to Br^-.

Quantitative analyses of the electronic structures and chemical properties of $Cs_2AgBiCl_6$ and $Cs_2AgBiBr_6$ NCs were performed by the combination of XPS and STEM-EDS analysis. The binding energies of XPS spectra were calibrated according to the signal of the C1s spectrum. **Figure 2** shows the survey and narrow scan XPS spectra of NCs. The spectra color-coded with red and blue represent $Cs_2AgBiCl_6$ and $Cs_2AgBiBr_6$ NCs, respectively. **Figure 2(a)** confirms the elemental composition of $Cs_2AgBiCl_6$ with the presence of peaks of Cs, Ag, Bi, Cl, and $Cs_2AgBiBr_6$ NCs with the presence of peaks of Cs, Ag, Bi, and Br. In the case of $Cs_2AgBiCl_6$ NCs, the Cs3d doublet peaks for $Cs_2AgBiCl_6$ NCs detected at 738.0 eV ($Cs3d_{3/2}$) and 724.0 eV ($Cs3d_{5/2}$) correspond to the standard Cs element, as shown in **Figure 2(b)**. The two peaks were disjoint with an energy value of 14 eV. **Figure 2(c)** exhibits the Ag3d XPS spectra of $Cs_2AgBiCl_6$ NCs with peaks at 373.8 eV ($Ag3d_{3/2}$) and 367.8 eV ($Ag3d_{5/2}$) associated with a monovalent oxidation state of Ag. The two peaks have an energy difference of 6 eV. The $Bi4f_{5/2}$ and $Bi4f_{7/2}$ peaks were located at 164.5 eV and 159.1 eV, as seen in **Figure 2(d)**. Additional Bi peaks with lower binding energy were observed at 161.6 eV and 156.5 eV corresponding to the low valence state $Bi^{(3-x)+}$, suggesting the formation of chlorine vacancies.[42] At the binding energy of 199.1 eV and 197.6 eV, the Cl2p peak can be divided into two peaks originating from $Cl2p_{1/2}$ and $Cl2p_{3/2}$, respectively (**Figure 2e**). In the case of $Cs_2AgBiBr_6$ NCs, **Figure 2(f)** shows the Br3d doublet peaks at 68.9 eV and 68.0 eV which are attributed to $Br3d_{3/2}$ and $Br3d_{5/2}$, respectively. Compared the $Cs_2AgBiBr_6$ to the $Cs_2AgBiCl_6$, the peak of Cs3d and Ag3d shift 0.2 eV toward higher binding energy, while the shift of Bi4f is smaller (0.15 eV), which indicates that the X-Br (X = Cs, Ag, Bi) interactions in $Cs_2AgBiBr_6$ are stronger than the X-Cl (X = Cs, Ag, Bi) interactions in $Cs_2AgBiCl_6$, meanwhile, the Bi-Cl interactions are weaker than Cs-Cl and Ag-Cl. The UV-VIS spectroscopy was utilized to evaluate the optical properties and light absorption capability of the $Cs_2AgBiCl_6$ and $Cs_2AgBiBr_6$ NCs as shown in **Figure 3(a)**. The absorption peaks account for the effective absorption of photons, which is potential for the capture of photocurrents of the photodiodes based on NCs. The sharp absorption peaks at around 368 nm and 425 nm are originated from the hybrid orbital of Bi6s/Ag4d defect level.[43] The optical bandgaps were estimated from the absorption spectra by using Tauc's plot method,[44,45] as shown in the inset of **Figure 3(a)**, red and blue dash lines are the tangent lines of the $(\alpha h\nu)^{1/n}$, where α is the absorption coefficient, h is Plank's constant, ν is the frequency of light, and the index $n = 2$ is related to the bandgap of indirect allowed transition semiconductors. The estimated bandgaps of the $Cs_2AgBiCl_6$ and $Cs_2AgBiBr_6$ NCs are 3.17 eV and 2.66 eV, respectively. In order to obtain information on the energy band for further application, the valence band minimum (VBM) and conduction band maximum (CBM) of the NCs were determined by using UPS. The UPS spectra of the secondary electron cutoff and valence band edge regions of both thin films are shown in **Figure 3(b)**. The work function

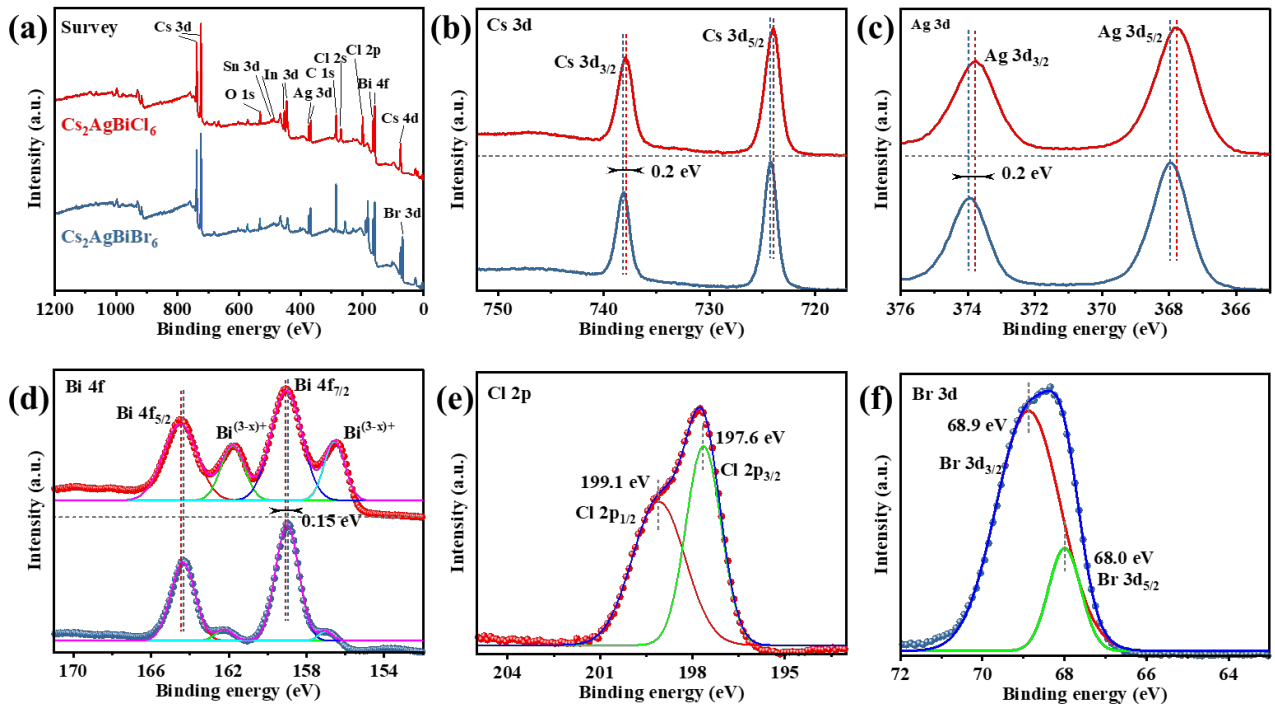

Figure 2. XPS spectra of (a) wide scan, (b) Cs 3d, (c) Ag 3d, (d) Bi 4f, (e) Cl 2p, (f) Br 3d core level obtained for $Cs_2AgBiCl_6$ (red line/scatter) and $Cs_2AgBiBr_6$ (blue line/scatter) NCs. All the spectra are calibrated to 284.8 eV, corresponding to C 1s peak.

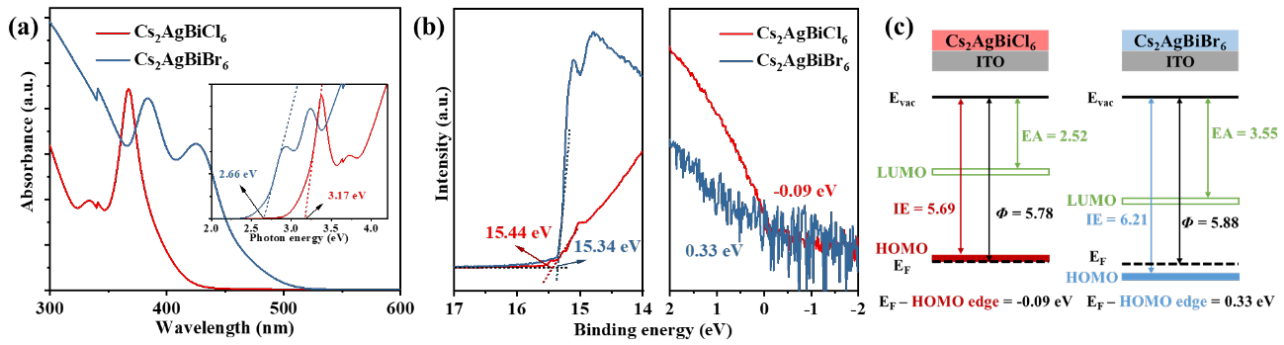

Figure 3. (a) UV-VIS spectra and Tauc plot of $Cs_2AgBiCl_6$ and $Cs_2AgBiBr_6$ NCs. (b) UPS spectra of $Cs_2AgBiCl_6$ and $Cs_2AgBiBr_6$ thin film. The left shows the cutoff of energy, and the right figure shows the enlarged spectral parts near the Fermi edge. (c) Energy level diagrams showing the results for $Cs_2AgBiCl_6$ and $Cs_2AgBiBr_6$ NCs on an ITO substrate. All energy values are scaled to eV, EA: electron affinity, IE: ionization energy, EF: fermi level, Φ: work function.

is calculated by the difference in energy between the secondary electron cutoff and the the excitation photon energy ($h\upsilon$ = 21.22 eV). The low and high binding energy cutoff regions of the UPS spectra are -0.09 eV (C_{onsest}) and 15.44 eV ($cutoff_{high}$) for the $Cs_2AgBiCl_6$ and 0.33 eV (C_{onset}) and 15.34 eV ($cutoff_{high}$) for the $Cs_2AgBiBr_6$, respectively. The energy level of $Cs_2AgBiCl_6$ NCs are -2.52 ~ -5.69 eV, and that of $Cs_2AgBiBr_6$ NCs is -3.55 ~ -6.21 eV, as shown in **Figure 3(c)**. To examine the optoelectronic properties of photodiodes based on $Cs_2AgBiCl_6$ and $Cs_2AgBiBr_6$ NCs in our work, devices based on $Cs_2AgBiCl_6$, $Cs_2AgBiBr_6$, $Cs_2AgBiBr_6$/PCBM were fabricated, and their photo-response were measured using the same procedure. **Figure 4(a)-(b)** showed the device configuration and the energy band diagram of photodiodes based on $Cs_2AgBiCl_6$ NCs under voltage unbiased conditions. Electrons and holes as separated charge carriers are promoted by built-in electric field offered by the energy difference between the functional layers. In the multilayer, by utilizing the type-II band alignment between ZnO and the perovskite NC layers, electrons and holes could

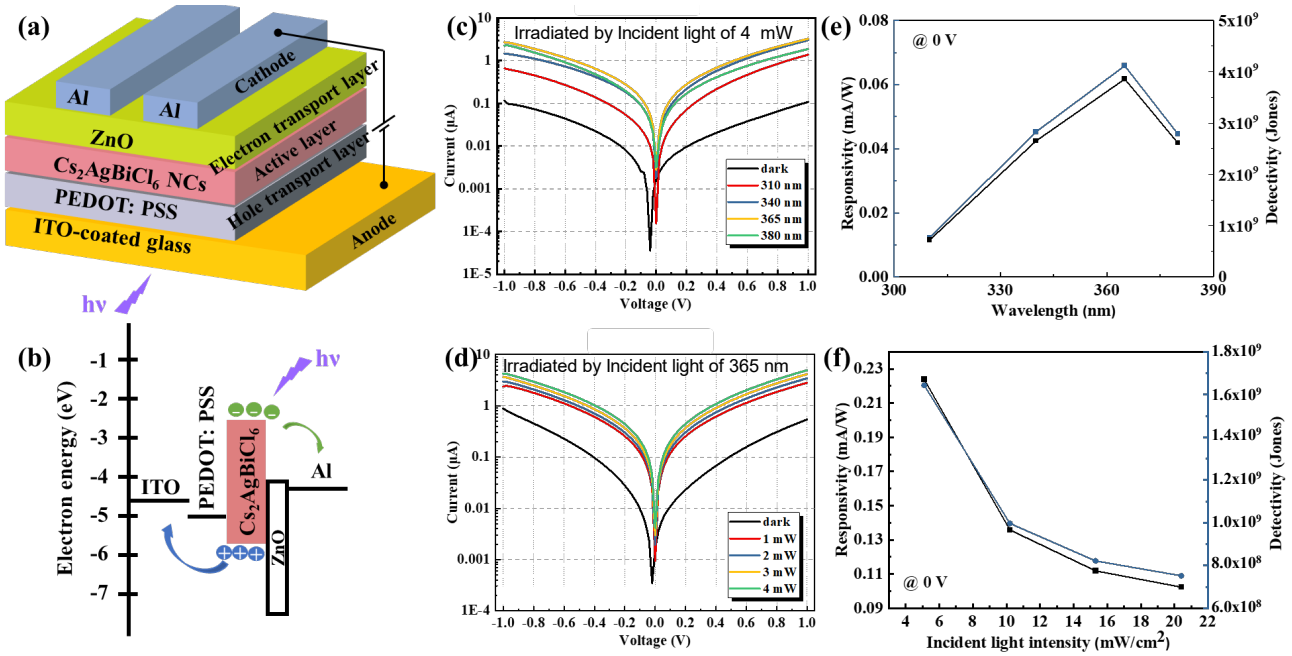

Figure 4. (a) Device configuration of photodiodes based on $Cs_2AgBiCl_6$ NCs. (b) The energy level which is corresponding to the device structure. The green and blue arrows indicate the moving direction of electron and hole, respectively. (c) Current versus applied voltage of photodiodes irradiated by incident light with different wavelength. (d) Current versus applied voltage of photodiodes irradiated by 365 nm incident light with different power intensities. (e) Responsivity and detectivity versus the wavelength of incident light under a bias voltage of 0 V. (f) Responsivity and detectivity versus incident light intensity of photodiode at a bias voltage of 0 V under 365 nm illumination.

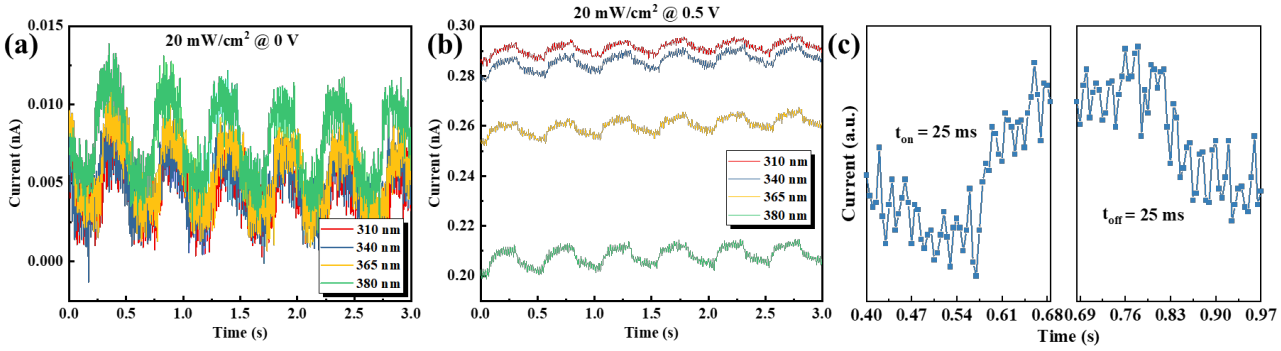

Figure 5. Dynamic current-time response of the photodiode under bias voltages of 0 V (a) and 0.5 V (b). (c) Enlarged spectra of the rise time and fall time of the photodiode under the illumination of 365 nm.

separate on ultrafast time scales for detection. **Figure 4(c)** shows the I-V characteristics of the $Cs_2AgBiCl_6$-based PDs while varying the wavelength of incident light between 310 nm and 380 nm. The incident light intensity was fixed at 4 mW par a same irradiated area. As shown in the figure, the device featured a pronounced photo-response at both forward and reverse bias of voltage. Obviously, photocurrent was detected under light irradiation. The generated photocurrent enhanced the built-in electric field and separate the electron-hole pairs. In the figure, the photocurrent was the highest at 365 nm light irradiation but tended to decrease with irradiation of even longer wavelengths. This wavelength dependency was consistent with the optical absorption behaviour in Figure 3(a). **Figure 4(d)** shows the I-V characteristics under 365-nm light irradiation while varying the photon power from 1 mW to 4 mW. It was observed that the photocurrent was dependent of the photon power by almost same increment. The photocurrent under a bias voltage of 0 V was about twice larger than the dark current under the 365 nm illumination. As the typical figure-of-merits, responsivity (R) and specific detectivity (D^*) identify the ability of a photodetector responding to a light radiation, and which level of light intensity can be detected, respectively.[46] R is expressed by $R = (I_{light} - I_{dark})/P_{in}$, where P_{in} represents the incident light power.[47,48] The specific

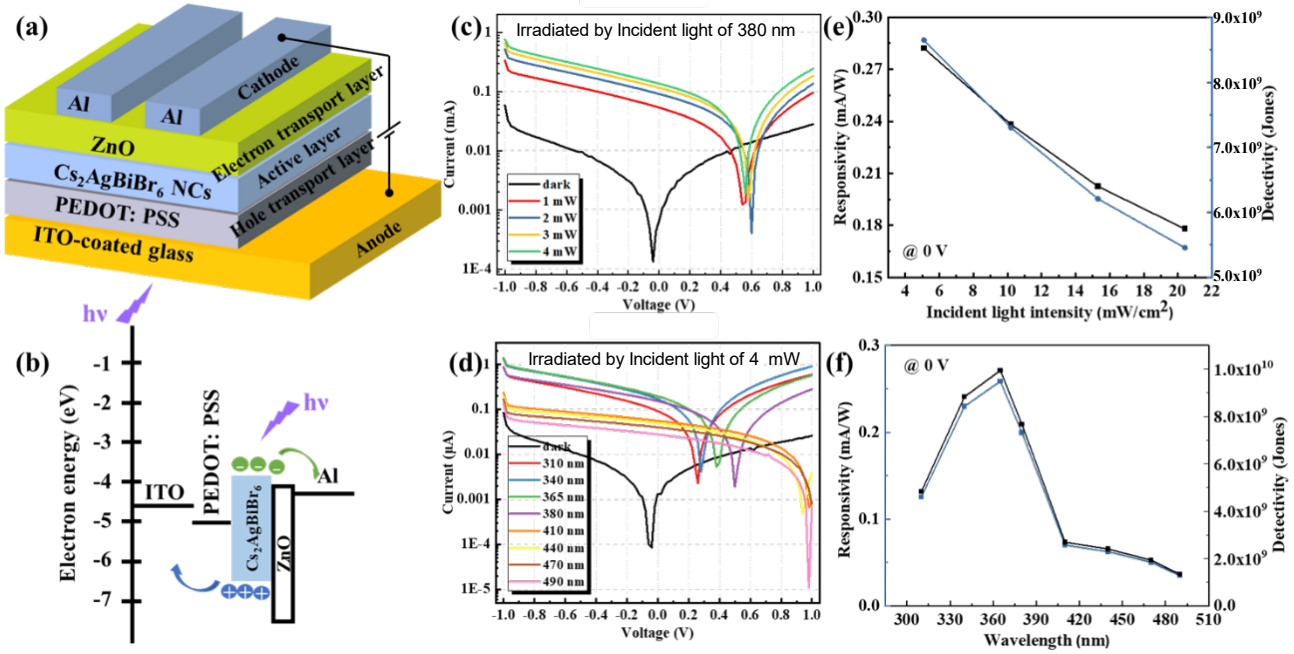

Figure 6. (a) Device configuration of photodiodes based on $Cs_2AgBiBr_6$ NCs. (b) The energy level which is corresponding to the device structure. (c) Current versus applied voltage of photodiodes irradiated by 380 nm incident light with different power intensities. (d) Current versus applied voltage of photodiodes irradiated by incident light with different wavelength. (e) Responsivity and detectivity versus incident light intensity of photodiode under a bias voltage of 0 V. (f) Responsivity and detectivity versus the wavelength of incident light under a bias voltage of 0 V.

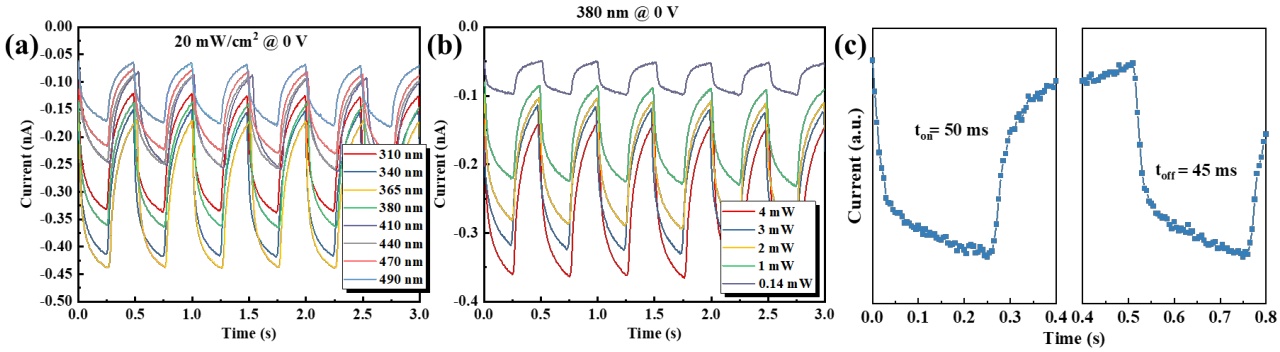

Figure 7. (a) Dynamic current-time response of the photodiode under a bias voltage of 0 V irradiated by the incident light with different wavelength. (b) Dynamic current-time response of the photodiode under a bias voltage of 0 V irradiated by the 380 nm light with different power intensity. (c) Enlarged spectra of the rise time and fall time of the photodiode irradiated by the 0.14 mW of 380 nm light measured under a bias voltage of 0 V.

detectivities were calculated on account of measured photocurrent, dark current, and incident light intensity which extracted from the equation $D^* = R_\lambda(S/(2qI_{dark}))^{1/2}$, where R_λ is the responsivity at a specific wavelength, the absolute charge value of electron is q, and S represents the effective irradiation area. [49] As shown in **Figure 4(e)-(f)**, R_A and D^* of PD were achieved, it showed 0.22 mA/W of responsivity and 1.7×10^9 Jones of detectivity under 365 nm illumination at a bias voltage of 0 V. As shown in **Figure 5**, the wavelength-dependent time-resolved response characteristics demonstrate on/off switching under radiation at 310, 340, 365, and 380 nm, respectively, at bias voltages of (a) 0 V (a) and (b) 0.5 V. Rise and fall times are regarded as the period time for dark current increase to the 90% of the maximal photocurrent and photocurrent drop to 10% of the maximal value. The response speed of device was 25 and 25 msec of rise and fall time, respectively. When the active layer changed from $Cs_2AgBiCl_6$ NCs to $Cs_2AgBiBr_6$ NCs, the device exhibits different performance. **Figure 6(a)-(b)** shows the device configuration and the energy band diagram of photodiodes based on $Cs_2AgBiBr_6$ NCs under voltage unbiased conditions. **Figure 6(c)** shows the I-V characteristics of PDs while varying

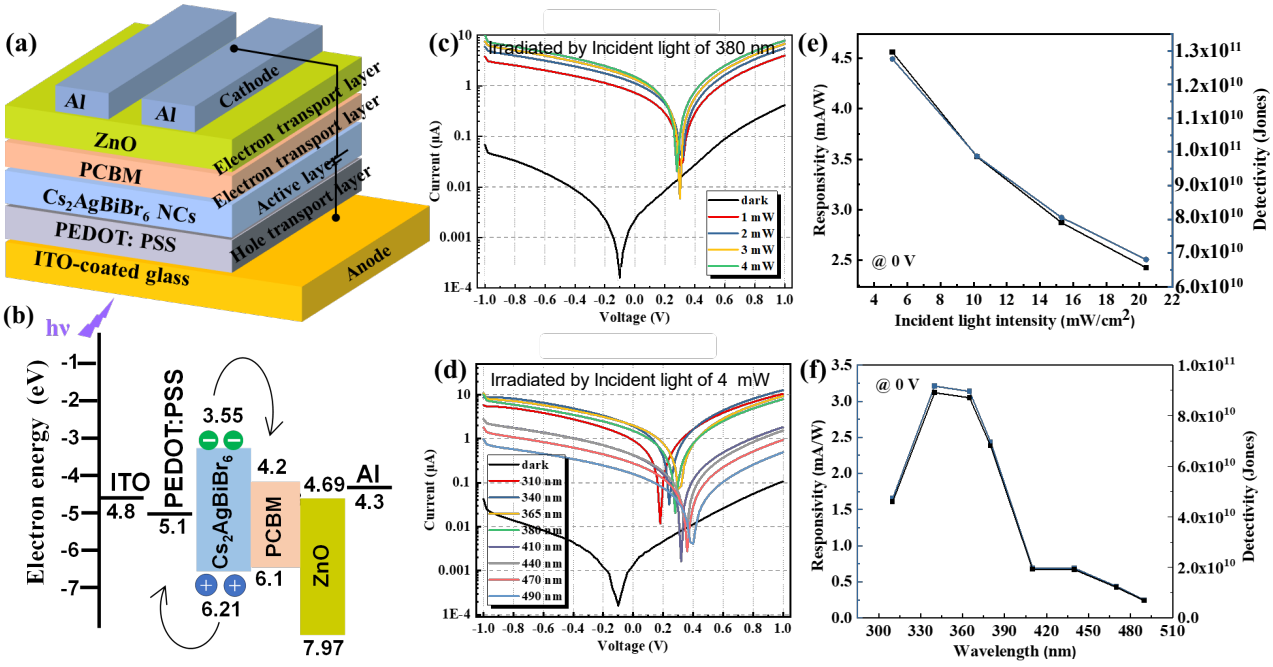

Figure 8. (a) Device configuration of photodiodes based on $Cs_2AgBiBr_6$ NCs with PCBM inserting layer. (b) The energy level which is corresponding to the device structure. (c) Current versus applied voltage of photodiodes irradiated by 380 nm incident light with different power intensities. (d) Current versus applied voltage of photodiodes irradiated by 4 mW incident light with different wavelength. (e) Responsivity and detectivity versus incident light intensity of photodiode under a bias voltage of 0 V. (f) Responsivity and detectivity versus the wavelength of incident light under a bias voltage of 0 V.

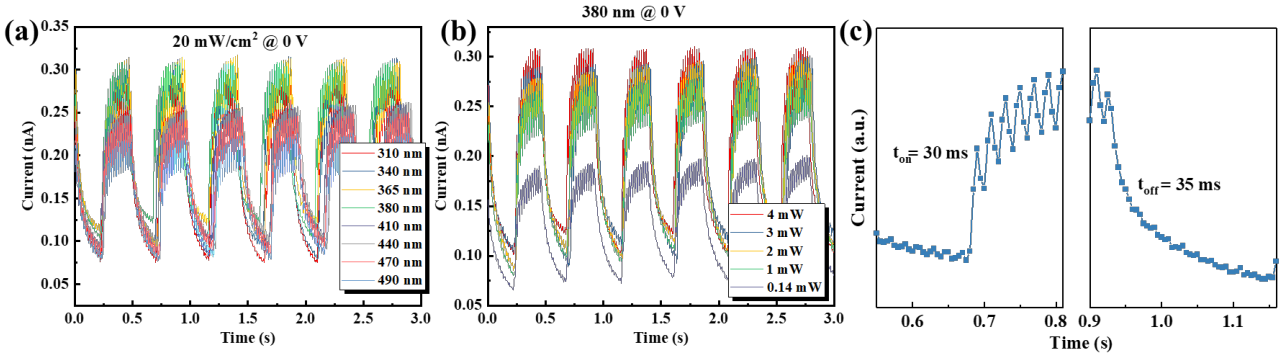

Figure 9. (a) Dynamic current-time response of the photodiode under a bias voltage of 0 V irradiated by the incident light with different wavelength. (b) Dynamic current-time response of the photodiode under a bias voltage of 0 V when irradiated by the 380 nm light with different power intensity. (c) Enlarged spectra of the rise time and fall time of the photodiode irradiated by the 0.14 mW of 380 nm light measured at a bias voltage of 0 V.

incident light intensity from 1 to 4 mW. It was observed that the light current intensity is in scale with the incident power density, consistent with the case of PD with $Cs_2AgBiCl_6$. The device showed significant photovoltaic effects with a maximum open circuit voltage (V_{oc}) of ~0.6 V. **Figure 6(d)** shows I-V characteristics measured at 4 mW while varying incident light wavelength between 310 nm and 490 nm. The highest photocurrent was obtained under 365 nm illumination whereas the photocurrent was the lowest under 490 nm illumination. The photocurrent difference between 365 nm and 490 nm might appear due to the absorbance difference between two wavelengths as shown in **Figure 3(a)**. For the $Cs_2AgBiBr_6$ NCs-based PD, the photocurrent under a bias voltage of 0 V was around 50 time larger than the dark current under the 365 nm illumination. As shown in **Figure 6(e)-(f)**, *R* and *D** of PD were achieved, it showed 0.27 mA/W of responsivity and 9.94×10^9 Jones of detectivity under 380 nm illumination at a bias voltage of 0 V. These values were higher than those of $Cs_2AgBiCl_6$ NCs-based PD, which might be attributed to the less defect density of $Cs_2AgBiBr_6$ NCs and more efficient separation of electron-hole pairs. The wavelength dependent time-resolved response characters are shown in **Figure 7(a)**, which indicates on/off switched properties under different illumination wavelength ranging from 310 to 490 nm at a bias voltage of 0 V. The photon power of the light was controlled to 20 mW/cm^2.The wavelength-dependent response was consistent with the result shown in **Figure 6(f)**. The on/off switched characteristics shown in **Figure 7(b)** were measured at a bias voltage of 0 V while varying photon power of incident light of 380 nm from 0.14 mW to 4 mW. **Figure 7(c)** exhibits a portion extracted from Figure 7(b). The response rise/fall time of device were 50/45 msec. The responsivity and detectivity were improved when compared to the device performance of $Cs_2AgBiCl_6$ NCs-based PD, but the response was a little slower. Generally, the NCs has the potential of quenching resulted from the interface defects, thus generating the trap which captures the carriers and slow the response. Further study is needed to determine the possible structural parameters that are responsible for defect formation.

Interface engineering is an effective strategy to enhance the carrier transportation between adjacent nanocrystals. Here the PCBM was used as an interface modifier, [50] and was inserted between the active layer and ZnO layer. In this work, we used the PD with $Cs_2AgBiBr_6$ that exhibited the better performance than the device based on $Cs_2AgBiCl_6$. **Figure 8(a)-(b)** shows the device configuration and energy band diagram of photodiodes based on the $Cs_2AgBiBr_6$/PCBM under voltage unbiased conditions. The I-V curves of the device under various incident power densities were shown in Figure 8(c). The incident light wavelength was fixed at 380 nm. As expected, the photogenerated current density increased with incident light intensity. Clearly, the device exhibited the photo voltaic characteristics and the V_{oc} has almost saturated at the measured minimum intensity of 1 mW. **Figure 8(d)** shows the I-V curves of PDs while varying the incident light wavelength between 310 nm and 490 nm. For the PCBM-modified PD, the photocurrent under a bias voltage of 0 V was around 150 time larger than the dark current under the 365 nm illumination. As shown in **Figure 8(e)-(f)**, we obtained a 3.21 mA/W of responsivity and an 8.91×10^{10} Jones of detectivity when irradiated with 340-nm light at a bias voltage of 0 V. These values were much higher than those of non-modified $Cs_2AgBiBr_6$ NCs-based PD, possibly because the presence of PCBM creates a continuous gradient band structure as shown in Figure 8(b). **Figure 9(a)** exhibited the dynamic responses, which indicates on/off switched properties when irradiated with light of wavelengths from 310 to 490 nm at a bias voltage of 0 V. The photon power of incident light was tuned to 20 mW/cm^2. The wavelength-dependent response was consistent with the result shown in **Figure 8(f)**. **Figure 9(b)** shows the time dependent photo responses of the $Cs_2AgBiBr_6$/PCBM-

Table 1. Comparison of the device performance of UV photodetectors based on $Cs_2B(I)B'(III)X_6$ crystals reported in literatures (B=Ag or Na; B'= Bi or In; X= Cl or Br).

Material	Shape	Responsivity R (mA/W)	Detectivity D^* (Jones)	Response speed (msec)	References
$Cs_2AgBiBr_6$	2D nanosheet	110 at 0 V	2×10^{10} at 0 V	3	51
$Cs_2AgBiCl_6$	2D nanosheet	9.68 at 0 V	1.11×10^{12} at 0 V	-	11
$Cs_2AgInCl_6$	Single crystal	13 at 5V	9.6×10^{11} at 5 V	~1.0	52
$Cs_2NaBiCl_6$	2D nanosheet	67.98 at 1.5 V	4.17×10^{11} at 1.5 V	16.82	53

based PD at a bias voltage of 0 V. Clearly the reproducible photocurrent response with a good cycling stability is observed. In addition, the PD responses to the UV-light with photon power as small as 0.14 mW. The photocurrent increases successively upon increasing the light irradiance power from 0.14 mW to 4 mW. **Figure 9(c)** exhibits on/off switched properties under radiation of 380 nm with different power intensity under a bias voltage of 0 V. The response rise/fall times of device were improved to 30/35 msec, respectively, which are faster than non-modified PDs (response speed of 50/45 msec). **Table 1** shows a summary of the device performances of photodetectors using different forms of crystalline $Cs_2B(I)B'(III)X_6$ (B=Ag or Na; B'=Bi or In; X= Cl or Br) as optical absorption layers. There are some advantages of using perovskite crystals as the optical absorption layer for optoelectronic applications instead of semiconductor quantum dots (QDs). First, there is no need to create a core-shell structure that requires skillful synthesis. Second, for QDs it has been common replace the long ligands used for synthesis with short ligands or ions to increase the packing density of QDs in the active layer, thereby appearing the photoresponse property.[54,55] In our case, the nanocrystals' surfaces were terminated with long ligands such as OA and OLA for colloidal stability. Nevertheless, it should be noted that our active layer exhibits good photoresponsive features. Compared to the reported performance of devices operated at a bias voltage of 0 V shown in Table 1, our device was somewhat less responsivity and detectivity, with a response time that is an order of magnitude slower. This is probably due to the large interparticle distance created by the organic ligands, which reduces carrier mobility. To enhance the device performance, the carrier mobility must be increased based on the strategy of interface engineering. Furthermore, the energy loss that occurs before the incident light reaches the light absorbing layer must be minimized. For example, the use of quarts glass covered with transparent electrode with a large bandgap such as SnO_2 is one of the procedures.

Conclusion

The photodiodes based on $Cs_2AgBiCl_6$ lead-free double perovskite NCs were prepared in our work which peculiarities proved to be promising by advantages of the simple composition engineering for halogen atoms to be replaced by the Br atoms from Cl atoms. The $Cs_2AgBiBr_6$ NCs with narrower bandgap were successfully synthesized which achieved the wavelength-selectivity when applied in photodiodes, additionally enhance the device performance. On the other hand, PCBM thin layer was inserting as an electron transport layer, the optimized photodiode exhibited a good self-powered performance which acted as the responsivity of 3.21 mA/W when the specific detectivity approached 8.91×10^{10} Jones, and a large light/dark current ratio near 200 was obtained. More importantly, spectral wavelength selectivity of $Cs_2AgBiBr_6$ NCs-based photodetector manifested the potential utilization in ultraviolet detecting, which point out potential application of lead-free double perovskite nanocrystals in next-generation photodiodes.

Acknowledgements

The authors thank Dr. OHSAWA Takeo of NIMS for technical support of the UPS measurements. This work was supported by JSPS KAKENHI Grant-in-Aid for Scientific Research (B) (Grant Numbers 21H01910 and 21H01743).

References

[1] Dou L, Yang Y (Micheal), You J, Hong Z, Chang W-H, Li G and Yang Y 2014 Solution-processed hybrid perovskite photodetectors with high detectivity *Nat. Commun.* **5** 5404

[2] Zhang W, Eperon G E and Snaith H J 2016 Metal halide perovskites for energy applications *Nat. Energy* **1** 16048

[3] Chen Q, Zhou H, Hong Z, Luo S, Duan H-S, Wang H-H, Liu Y, Li G and Yang Y 2014 Planar Heterojunction Perovskite Solar Cells via Vapor-Assisted Solution Process *J. Am. Chem. Soc.* **136** 622–625

[4] Li X, Bi D, Yi C, Décoppet J-D, Luo J, Zakeeruddin S M, Hagfeldt A and Grätzel M 2016 A vacuum flash–assisted solution process for high-efficiency large-area perovskite solar cells *Science (80-.).* **353** 58–62

[5] Leung S-F, Ho K-T, Kung P-K, Hsiao V K S, Alshareef H N, Wang Z L and He J-H 2018 A Self-Powered and Flexible Organometallic Halide Perovskite Photodetector with Very High Detectivity *Adv. Mater.* **30** 1704611

[6] Stranks S D, Eperon G E, Grancini G, Menelaou C, Alcocer M J P, Leijtens T, Herz L M, Petrozza A and Snaith H J 2013 Electron-Hole Diffusion Lengths Exceeding 1 Micrometer in an Organometal Trihalide Perovskite Absorber *Science (80-.).* **342** 341–344

[7] De Roo J, Ibáñez M, Geiregat P, Nedelcu G, Walravens W, Maes J, Martins J C, Van Driessche I, Kovalenko M V and Hens Z 2016 Highly Dynamic Ligand Binding and Light Absorption Coefficient of Cesium Lead Bromide Perovskite Nanocrystals *ACS Nano* **10** 2071–2081

[8] Shi D, Adinolfi V, Comin R, Yuan M, Alarousu E, Buin A, Chen Y, Hoogland S, Rothenberger A, Katsiev K, Losovyj Y, Zhang X, Dowben P A, Mohammed O F, Sargent E H and Bakr O M 2015 Low trap-state density and long carrier diffusion in organolead trihalide perovskite single crystals *Science (80-.).* **347** 519–522

[9] Lin Q, Armin A, Lyons D M, Burn P L and Meredith P 2015 Low Noise, IR-Blind Organohalide Perovskite Photodiodes for Visible Light Detection and Imaging *Adv. Mater.* **27** 2060–2064

[10] Zhumekenov A A, Saidaminov M I, Haque M A, Alarousu E, Sarmah S P, Murali B, Dursun I, Miao X-H, Abdelhady A L, Wu T, Mohammed O F and Bakr O M 2016 Formamidinium Lead Halide Perovskite Crystals with Unprecedented Long Carrier Dynamics and Diffusion Length *ACS Energy Lett.* **1** 32–37

[11] Wang M, Zeng P, Wang Z and Liu M 2020 Vapor-Deposited $Cs_2AgBiCl_6$ Double Perovskite Films toward Highly Selective and Stable Ultraviolet Photodetector *Adv. Sci.* **7** 1903662

[12] Lei H, Hardy D and Gao F 2021 Lead-Free Double Perovskite $Cs_2AgBiBr_6$: Fundamentals, Applications, and Perspectives *Adv. Funct. Mater.* **31** 2105898

[13] Volonakis G, Haghighirad A A, Milot R L, Sio W H, Filip M R, Wenger B, Johnston M B, Herz L M, Snaith H J and Giustino F 2017 $Cs_2InAgCl_6$: A New Lead-Free Halide Double Perovskite with Direct Band Gap *J. Phys. Chem. Lett.* **8** 772–778

[14] Zhou J, Rong X, Molokeev M S, Zhang X and Xia Z 2018 Exploring the transposition effects on the electronic and optical properties of $Cs_2AgSbCl_6$via a combined computational-experimental approach *J. Mater. Chem. A* **6** 2346–2352

[15] Filip M R and Giustino F 2016 Computational Screening of Homovalent Lead Substitution in Organic–Inorganic Halide Perovskites *J. Phys. Chem. C* **120** 166–173

[16] Zhao X-G, Yang J-H, Fu Y, Yang D, Xu Q, Yu L, Wei S-H and Zhang L 2017 Design of Lead-Free Inorganic Halide Perovskites for Solar Cells via Cation-Transmutation *J. Am. Chem. Soc.* **139** 2630–2638

[17] Yan D-N, Liao C-S, Zhao Y-Q, Liu B, Yang J-L and Cai M-Q 2020 Theoretical prediction of double perovskite $Cs_2AgxCu_{1-x}InyTb_{1-y}Cl_6$ for infrared detection *J. Phys. D. Appl. Phys.* **53** 265302

[18] Lamba R S, Basera P, Singh S, Bhattacharya S and Sapra S 2021 Lead-Free Alloyed Double-Perovskite Nanocrystals of $Cs_2(Na_xAg_{1-x})BiBr_6$ with Tunable Band Gap *J. Phys. Chem. C* **125** 1954–1962

[19] Ning W, Wang F, Wu B, Lu J, Yan Z, Liu X, Tao Y, Liu J-M, Huang W, Fahlman M, Hultman L, Sum T C and Gao F 2018 Long Electron–Hole Diffusion Length in High-Quality Lead-Free Double Perovskite Films *Adv. Mater.* **30** 1706246

[20] Zheng Y, Luo F, Ruan L, Tong J, Yan L, Sun C and Zhang X 2022 A facile fabrication of lead-free Cs_2NaBiI_6 double perovskite films for memory device application *J. Alloys Compd.* **909** 164613

[21] Soni A, Bhamu K C and Sahariya J 2020 Investigating effect of strain on electronic and optical properties of lead free double perovskite $Cs_2AgInCl_6$ solar cell compound: A first principle calculation *J. Alloys Compd.* **817** 152758

[22] Mo Q, Yu J, Chen C, Cai W, Zhao S, Li H and Zang Z 2022 Highly Efficient and Ultra-Broadband Yellow Emission of Lead-Free Antimony Halide toward White Light-Emitting Diodes and Visible Light Communication *Laser Photon. Rev.* **16** 2100600

[23] Yang X, Wang W, Ran R, Zhou W and Shao Z 2020 Recent Advances in $Cs_2AgBiBr_6$-Based Halide Double Perovskites as Lead-Free and Inorganic Light Absorbers for Perovskite Solar Cells *Energy & Fuels* **34** 10513–10528

[24] Slavney A H, Hu T, Lindenberg A M and Karunadasa H I 2016 A Bismuth-Halide Double Perovskite with Long Carrier Recombination Lifetime for Photovoltaic Applications *J. Am. Chem. Soc.* **138** 2138–2141

[25] Kentsch R, Scholz M, Horn J, Schlettwein D, Oum K and Lenzer T 2018 Exciton Dynamics and Electron–Phonon Coupling Affect the Photovoltaic Performance of the $Cs_2AgBiBr_6$ Double Perovskite *J. Phys. Chem. C* **122** 25940–25947

[26] Biega R-I, Filip M R, Leppert L and Neaton J B 2021 Chemically Localized Resonant Excitons in Silver–Pnictogen Halide Double Perovskites *J. Phys. Chem. Lett.* **12** 2057–2063

[27] Lan Z, Lau Y S, Cai L, Han J, Suen C W and Zhu F 2022 Dual-Band Organic Photodetectors for Dual-Channel Optical Communications *Laser Photon. Rev.* **16** 2100602

[28] Yan G, Jiang B, Xiao Y, Zhao C, Yuan Y and Liang Z 2022 Alkali metal ions induced high-quality all-inorganic Cs2AgBiBr6 perovskite films for flexible self-powered photodetectors *Appl. Surf. Sci.* **579** 152198

[29] Elsinger L, Petit R, Van Acker F, Zawacka N K, Tanghe I, Neyts K, Detavernier C, Geiregat P, Hens Z and Van Thourhout D 2021 Waveguide-Coupled Colloidal Quantum Dot Light Emitting Diodes and Detectors on a Silicon Nitride Platform *Laser Photon. Rev.* **15** 2000230

[30] Zhang J, Wang C, Fu H, Gong L, He H, Fang Z, Zhou C, Chen J, Chao Z and Fan J 2021 Low-temperature preparation achieving 10.95%-efficiency of hole-free and carbon-based all-inorganic CsPbI3 perovskite solar cells *J. Alloys Compd.* **862** 158454

[31] Sivashanmugan K, Lin C-H, Hsu S-H, Guo T-F and Wen T-C 2018 Interfacial engineering of ZnO surface modified with poly-vinylpyrrolidone and p-aminobenzoic acid for high-performance perovskite solar cells *Mater. Chem. Phys.* **219** 90–95

[32] Ruankham P, Wongratanaphisan D, Gardchareon A, Phadungdhitidhada S, Choopun S and Sagawa T 2017 Full coverage of perovskite layer onto ZnO nanorods via a modified sequential two-step deposition method for efficiency enhancement in perovskite solar cells *Appl. Surf. Sci.* **410** 393–400

[33] Lee H-J and Na S-I 2022 Investigation of PCBM/ZnO and C60/BCP-based electron transport layer for high-performance p-i-n perovskite solar cells *J. Alloys Compd.* **921** 166007

[34] Liu G, Zhong Y, Mao H, Yang J, Dai R, Hu X, Xing Z, Sheng W, Tan L and Chen Y 2022 Highly efficient and stable ZnO-based MA-free perovskite solar cells via overcoming interfacial mismatch and deprotonation reaction *Chem. Eng. J.* **431** 134235

[35] Noh Y W, Jin I S, Kim K S, Park S H and Jung J W 2020 Reduced energy loss in SnO_2/ZnO bilayer electron transport layer-based perovskite solar cells for achieving high efficiencies in outdoor/indoor environments *J. Mater. Chem. A* **8** 17163–17173

[36] Ye J, Li Y, Medjahed A A, Pouget S, Aldakov D, Liu Y and Reiss P 2021 Doped Bilayer Tin(IV) Oxide Electron Transport Layer for High Open-Circuit Voltage Planar Perovskite Solar Cells with Reduced Hysteresis *Small* **17** 2005671

[37] Huang X, Matsushita Y, Sun H-T and Shirahata N 2022 Impact of bismuth-doping on enhanced radiative recombination in lead-free double-perovskite nanocrystals *Nanoscale Adv.* **4** 3091–3100

[38] Han P, Mao X, Yang S, Zhang F, Yang B, Wei D, Deng W and Han K 2019 Lead-Free Sodium–Indium Double Perovskite Nanocrystals through Doping Silver Cations for Bright Yellow Emission *Angew. Chemie - Int. Ed.* **58** 17231–17235

[39] Shirahata N, Yonezawa T, Seo W-S and Koumoto K 2004 Photoinduced Cleavage of Alkyl Monolayers on Si *Langmuir* **20** 1517–1520

[40] Gray M B, Majher J D, Strom T A and Woodward P M 2019 Broadband White Emission in $Cs_2AgIn_{1-x}Bix Cl_6$ Phosphors *Inorg. Chem.* **58** 13403–13410

[41] Ji F, Klarbring J, Wang F, Ning W, Wang L, Yin C, Figueroa J S M, Christensen C K, Etter M, Ederth T, Sun L, Simak S I, Abrikosov I A and Gao F 2020 Lead-Free Halide Double Perovskite $Cs_2AgBiBr_6$ with Decreased Band Gap *Angew. Chemie Int. Ed.* **59** 15191–15194

[42] Zhang G, Cai L, Zhang Y and Wei Y 2018 Bi5+, Bi(3−x)+, and Oxygen Vacancy Induced BiOClxI1−x Solid Solution toward Promoting Visible-Light Driven Photocatalytic Activity *Chem. – A Eur. J.* **24** 7434–7444

[43] Luo J, Wang X, Li S, Liu J, Guo Y, Niu G, Yao L, Fu Y, Gao L, Dong Q, Zhao C, Leng M, Ma F, Liang W, Wang L, Jin S, Han J, Zhang L, Etheridge J, Wang J, Yan Y, Sargent E H and Tang J 2018 Efficient and stable emission of warm-white light from lead-free halide double perovskites *Nature* **563** 541–545

[44] Manna D, Das T K and Yella A 2019 Tunable and Stable White Light Emission in Bi^{3+}-Alloyed Cs2AgInCl6 Double Perovskite Nanocrystals *Chem. Mater.* **31** 10063–10070

[45] Noculak A, Morad V, McCall K M, Yakunin S, Shynkarenko Y, Wörle M and Kovalenko M V 2020 Bright Blue and Green Luminescence of Sb(III) in Double Perovskite Cs_2MInCl_6 (M = Na, K) Matrices *Chem. Mater.* **32** 5118–5124

[46] Shen K, Xu H, Li X, Guo J, Sathasivam S, Wang M, Ren A, Choy K L, Parkin I P, Guo Z and Wu J 2020 Flexible and Self-Powered Photodetector Arrays Based on All-Inorganic $CsPbBr_3$ Quantum Dots *Adv. Mater.* **32** 2000004

[47] Li L, Chen H, Fang Z, Meng X, Zuo C, Lv M, Tian Y, Fang Y, Xiao Z, Shan C, Xiao Z, Jin Z, Shen G, Shen L and Ding L 2020 An Electrically Modulated Single-Color/Dual-Color Imaging Photodetector *Adv. Mater.* **32** 1907257

[48] Qian L, Sun Y, Sun M, Fang Z, Li L, Xie D, Li C and Ding L 2019 2D perovskite microsheets for high-performance photodetectors *J. Mater. Chem. C* **7** 5353–5358

[49] Wang Y, Yang Z, Li H, Li S, Zhi Y, Yan Z, Huang X, Wei X, Tang W and Wu Z 2020 Ultrasensitive Flexible Solar-Blind Photodetectors Based on Graphene/Amorphous Ga_2O_3 van der Waals Heterojunctions *ACS Appl. Mater. Interfaces* **12** 47714–47720

[50] Hewlett R M and McLachlan M A 2016 Surface Structure Modification of ZnO and the Impact on Electronic Properties *Adv. Mater.* **28** 3893–3921

[51] Wu C, Du B, Luo W, Liu Y, Li T, Wang D, Guo X, Ting H, Fang Z, Wang S, Chen Z, Chen Y and Xiao L 2018 Highly Efficient and Stable Self-Powered Ultraviolet and Deep-Blue Photodetector Based on $Cs_2AgBiBr_6/SnO_2$ Heterojunction. *Adv. Opt. Mater.* **6**, 1800811

[52] Luo J, Li S, Wu H, Zhou Y, Li Y, Liu J, Li J, Li K, Yi F, Niu G and Tang J 2018 $Cs_2AgInCl_6$ Double Perovskite Single Crystals: Parity Forbidden Transitions and Their Application For Sensitive and Fast UV Photodetectors *ACS Photon* **5**, 398-405

[53] Li H, Pi C, Chen W, Zhou M, Wei J, Yi J, Song P, Alexey Y, Zhong Y, Yu X, Qiu J and Xu X 2021 A Highly Stable Photodetector Based on a Lead-Free DoublePerovskite Operating at Different Temperatures *J. Phys. Chem. Lett.* **12**, 5682-5688

[54] Chatterjee S, Nemoto K, Ghosh B, Sun HT and Shirahata N 2023 Solution-Processed InSb Quantum Dot Photodiodes for Short-Wave Infrared Sensing *ACS Appl. Nano Mater.* **6** 15540-15550.

[55] Nemoto K, Watanabe J, Yamada H, Sun HT, Shirahata N, Impact of Coherent Core/Shell Architecture on Fast Response in InP-based Quantum Dot Photodiodes 2023 Impact of Coherent Core/Shell Architecture on Fast Response in InP-based Quantum Dot Photodiodes *Nanoscale Adv.* **5**, 907-915.